Distinguishing between Shock-darkening and Space-weathering Trends in Ordinary Chondrite Reflectance Spectra

Kohout, Tomas

2020-09-01

þÿ K o h o u t , T , P e n t t i l ä , A , M a n n , P , C l o u t i s , E , u d a , J , F i l i p , J , Grokhovsky , V I , Yakovlev , G A , Halodova , P & Haloda , J 2020 , ' Distinguishing between Shock-darkening and Space-weathering Trends in Ordinary Chondrite Reflectance Spectra ' , The Planetary Science Journal , vol. 1 , no. 2 , 37 . https://doi.org/10.3847/PSJ/aba7c2

http://hdl.handle.net/10138/324300
https://doi.org/10.3847/PSJ/aba7c2

The Planetary Science Journal, 1:37 (12pp), 2020 September https://doi.org/10.3847/PSJ/aba7c2

Distinguishing between Shock-darkening and Space-weathering Trends in Ordinary Chondrite Reflectance Spectra

Tomas Kohout[1,2], Antti Penttilä[3], Paul Mann[4], Ed Cloutis[4], Jan Čuda[5], Jan Filip[5], Ondrej Malina[5], Vishnu Reddy[6], Victor I. Grokhovsky[7], Grigoriy A. Yakovlev[7], Patricie Halodova[8], and Jakub Haloda[9]
[1] Institute of Geology, The Czech Academy of Sciences, Prague, Czech Republic; tomas.kohout@helsinki.fi
[2] Department of Geosciences and Geography, University of Helsinki, Finland
[3] Department of Physics, University of Helsinki, Finland
[4] Department of Geography, University of Winnipeg, Canada
[5] Regional Centre of Advanced Technologies and Materials, Palacký University Olomouc, Czech Republic
[6] Lunar and Planetary Laboratory, The University of Arizona, Tucson, AZ, USA
[7] Institute of Physics and Technology, Ural Federal University, Ekaterinburg, Russia
[8] Research Centre Řež, Husinec-Řež, Czech Republic
[9] Oxford Instruments NanoAnalysis, High Wycombe, Bucks, UK
Received 2020 April 8; revised 2020 June 14; accepted 2020 July 19; published 2020 August 19

Abstract

Space-weathering as well as shock effects can darken meteorite and asteroid reflectance spectra. We present a detailed comparative study on shock-darkening and space-weathering using different lithologies of the Chelyabinsk LL5 chondrite. Compared to space-weathering, the shock processes do not cause significant spectral slope changes and are more efficient in attenuating the orthopyroxene 2 μm absorption band. This results in a distinct shock vector in the reflectance spectra principal component analysis, moving the shocked silicate-rich Chelyabinsk spectra from the S-complex space into the C/X complex. In contrast to this, the space-weathering vector stays within the *S* complex, moving from Q type to S type. Moreover, the 2 μm to 1 μm band depth ratio (BDR) as well as the 2 μm to 1 μm band area ratio (BAR) are not appreciably affected by shock-darkening or shock melting. Space-weathering, however, causes significant shifts in both BDR and BAR toward higher values. Application of the BDR method to the three distinct areas on the asteroid Itokawa reveals that Itokawa is rather uniformly space-weathered and not influenced by regolith roughness or relative albedo changes.

Unified Astronomy Thesaurus concepts: Meteorites (1038); Chondrites (228)

1. Introduction

Space-weathering is a common process affecting the surfaces of airless bodies across our solar system. It is caused by a combination of the solar wind, micrometeorite bombardment, and galactic radiation, and it alters the physical, chemical, and crystallographic properties of surface materials (e.g., reviews by Hapke 2001; Bennett et al. 2013; Domingue et al. 2014; Pieters & Noble 2016). Space-weathering often causes changes in the visible (VIS), infrared (IR), and ultraviolet (UV) spectral regions, making it challenging to compare the weathered asteroidal and lunar spectra to those of unweathered minerals, meteorites (Britt et al. 1992; Lazzarin et al. 2006), and fresh lunar samples (Adams & Jones 1970; Hapke et al. 1970; Hapke 2001). The most prominent and well-documented space-weathering-induced spectral changes on both the Moon and asteroids are the lowering of albedo, suppression of mineral absorption bands, and changes in spectral slope (e.g., see reviews by Hapke 2001; Chapman 2004; Pieters & Noble 2016).

While on the Moon these spectral changes are often observed simultaneously, on the S-complex asteroids, they may occur at varying relative intensities (Chapman 2004; Hiroi et al. 2006; Gaffey 2010) due to the fact that main-belt asteroids are farther from the Sun, and therefore, the solar wind flux is dramatically lower than near the Moon. Also, the average impact velocities in the main asteroid belt are lower compared to the lunar vicinity. As learned from the Moon (Hapke et al. 1975) and later confirmed by numerous laboratory simulations (e.g., Sasaki et al. 2001; Marchi et al. 2005), the most optically important agent behind these spectral changes is the nanophase metallic iron particles (npFe^0) being generated by space-weathering through the reduction of Fe^{2+} ions in the surface layers of mineral grains. The presence of npFe^0 (accompanied by nanophase FeS) on S-complex near-Earth asteroids has been observed in the sample returned from the asteroid Itokawa by the JAXA Hayabusa mission (Noguchi et al. 2011). However, their presence on main-belt asteroids has to be still confirmed as their presence in meteorites is sparse (Noble et al. 2010).

Target mineralogy and iron content play important roles in the extent and rate of space-weathering in addition to the object's heliocentric distance. For example, laboratory experiments (Sasaki et al. 2002; Marchi et al. 2005) and atomic-scale simulations (Quadery et al. 2015) with olivine and orthopyroxene show that, compared to orthopyroxene of the same iron content, olivine requires approximately 50 times less energy input to exhibit similar spectral changes. Thus, under the assumption that these experiments accurately mimic space-weathering, the associated optical effects in olivine occur faster.

Shock-darkening related to impacts or asteroid collisions is another process capable of altering the reflectance spectra of planetary materials. This phenomenon is often observed in ordinary chondrites. Ordinary chondrites are dominated by silicates, and the spectra of olivine–orthopyroxene mixtures are

similar to S-complex asteroid members (DeMeo et al. 2009). In contrast, the spectra of shock-darkened ordinary chondrites are altered toward darker, featureless spectra resembling C/X-complex asteroids (Keil et al. 1992; Britt & Pieters 1994; Kohout et al. 2014b).

The shock-darkening mechanism as observed in meteorites is related to partial (troilite or FeNi metal) or complete material melting due to impact-related postshock heating (Heymann 1967; Smith & Goldstein 1977; Scott 1982; Rubin 1985, 1992). Two stages of darkening with distinct mechanisms are observed. First, troilite predominantly melts at moderate shock levels due to its lower melting point compared to iron (~1463 K versus ~1825 K) and is injected into silicate grains, forming a web of fine melt veins. Small amounts of silicate or metal melts are localized in thin shock veins. This happens in a rather narrow pressure range of ~40–50 GPa as determined through numerical simulations (Moreau et al. 2017, 2019) as well as experimentally (Kohout et al. 2020). Such a pressure range corresponds to a transition between shock stages C-S5 and C-S6 in the shock scale based on microscopic mineral shock features observed by Stoffler et al. (2018, 2019). We will refer to such material in this study as being shock-darkened (SD).

As reported recently in Kohout et al. (2020) through shock experiments with the Chelyabinsk meteorites, shock-darkening ceases at pressures over ~60 GPa due to the onset of silicate melting along grain or crack boundaries. The silicate and troilite melts are immiscible and thus, the troilite melt infusion into silicate grains is prevented by the silicate melt coating the residual solid silicate grains. Thus, the ordinary chondrite material retains to a large extent its bright appearance. With the progressive increase of postshock heating, the silicates melt gradually in larger proportions (Moreau et al. 2017), forming abundant impact-melt veins or pockets typical for shock stage C-S6.

The second darkening stage occurs at pressures over ~90–150 GPa (Kohout et al. 2020) associated with postshock temperatures over ~1800 K (Moreau et al. 2017) and bulk melting. The dark appearance of the material is related to the iron metal and troilite being finely dispersed within molten silicate material, forming spherical eutectic blebs (Andronikov et al. 2015). Such material corresponds to the shock stage C-S7, and we will refer to it in this study as impact melt (IM). Sometimes, the IM can retain a portion of finely brecciated unmelted silicates (Kohout et al. 2014b) or crystallize into new elongated prismatic olivine crystals surrounded by quenched residual silicate melt (Kaeter et al. 2018).

As the ordinary chondrite darkening is related to two distinct mechanisms with characteristic pressure regions separated by an interval where the darkening ceases, the amount of shock-darkened material produced during asteroid collisions may be reduced. The quantitative estimate of shock-darkened or impact-melted material exposed on asteroids is still a subject of discussion. While some work (Keil et al. 1992) suggest rather small amounts, relatively large-scale darkened IM breccia with floating clasts of unmolten material suggestive of extensive melt generation have been reported among the Chelyabinsk meteorites (e.g., Trieloff et al. 2018 or Grokhovsky et al. 2020)

At first look, the spectral effects of shock-darkening or impact-melting carry many of the characteristics of space-weathering. Shock-darkened meteorites can show an overall reduction in reflectance and suppression of silicate absorption bands. In comparison to space-weathering, minimal spectral slope changes have been observed in the shocked meteorites (Britt et al. 1989; Britt & Pieters 1994; Kohout et al. 2014b). The spectral slope, however, is not a unique indicator of space-weathering and may also change, for example, due to variations in phase angle, particle grain size, size of metallic inclusions, etc.

As both space-weathering and the shock-related darkening are processes capable of significantly darkening chondritic materials, a question arises—are we able to detect these individual processes in asteroid reflectance spectra and to distinguish between them?

While previous studies of shock-darkening have been focused on meteorites with the various above-mentioned shock features, no study to date has compared both partially or entirely shock-molten samples against their pristine and space-weathered low-shock equivalents originating from a single meteorite fall. To distinguish how the shock or space-weathering affect meteorite reflectance spectra, we investigated the Chelyabinsk LL5 chondrite. Chelyabinsk has the advantage of being a recent fall, with samples recovered soon after the fall (Popova et al. 2013; Kohout et al. 2014b), so that its terrestrial weathering has been minimal. Chelyabinsk also contains material with various levels of shock. In addition, being an LL5, it has similar mineralogy to the asteroid 25143 Itokawa, allowing us to relate our laboratory spectra to spectra acquired for Itokawa, which is also likely an LL chondrite (Abe et al. 2006).

Three powder mixture series of fusion crust-free samples of Chelyabinsk with increasing amount of shocked material and one series subjected to laboratory simulations of space-weathering were prepared, and their reflectance spectra were measured. Particular attention was paid to the behavior of the 1 μm and 2 μm silicate absorption bands, as these bands can manifest the response of different silicate minerals to shock and space-weathering. The 1 μm band is caused by the Fe^{2+} ions in both olivine (broad superposition of three individual overlapping bands) and orthopyroxene (single narrow band). The broad 2 μm band is caused by the Fe^{2+} ions in orthopyroxene (Burns 1970, 1993).

2. Materials and Methods

2.1. Meteorite Material

The 2013 Chelyabinsk meteorite fall (LL5) represents a unique material to study shock effects due to the availability of a large amount of fresh material of identical bulk composition, but with varying shock levels. The three basic lithologies (Figure 1) found among the Chelyabinsk meteorites are (1) lightly shocked light-colored lithology, (2) partly molten SD dark-colored lithology, and (3) entirely molten impact melt lithology. Andronikov et al. (2015), Galimov et al. (2013), Kaeter et al. (2018), Kohout et al. (2014b), Morlok et al. (2017), Moroz et al. (2014), and Righter et al. (2015) studied the above-mentioned lithologies in detail and assigned corresponding shock levels to them. The light-colored lithology shows evidence of a moderate shock level C-S4 with solid-state shock effects observed under polarized light in silicate grains and containing only sparse shock veins. The dark-colored lithology is characterized by extensive melting of troilite, which fills cracks within silicate grains and which is indicative of shock level C-S5-6. The IM lithology is predominantly composed of a whole-rock melt with finely brecciated silicate clasts and eutectic troilite-metal blebs and thus can be assigned

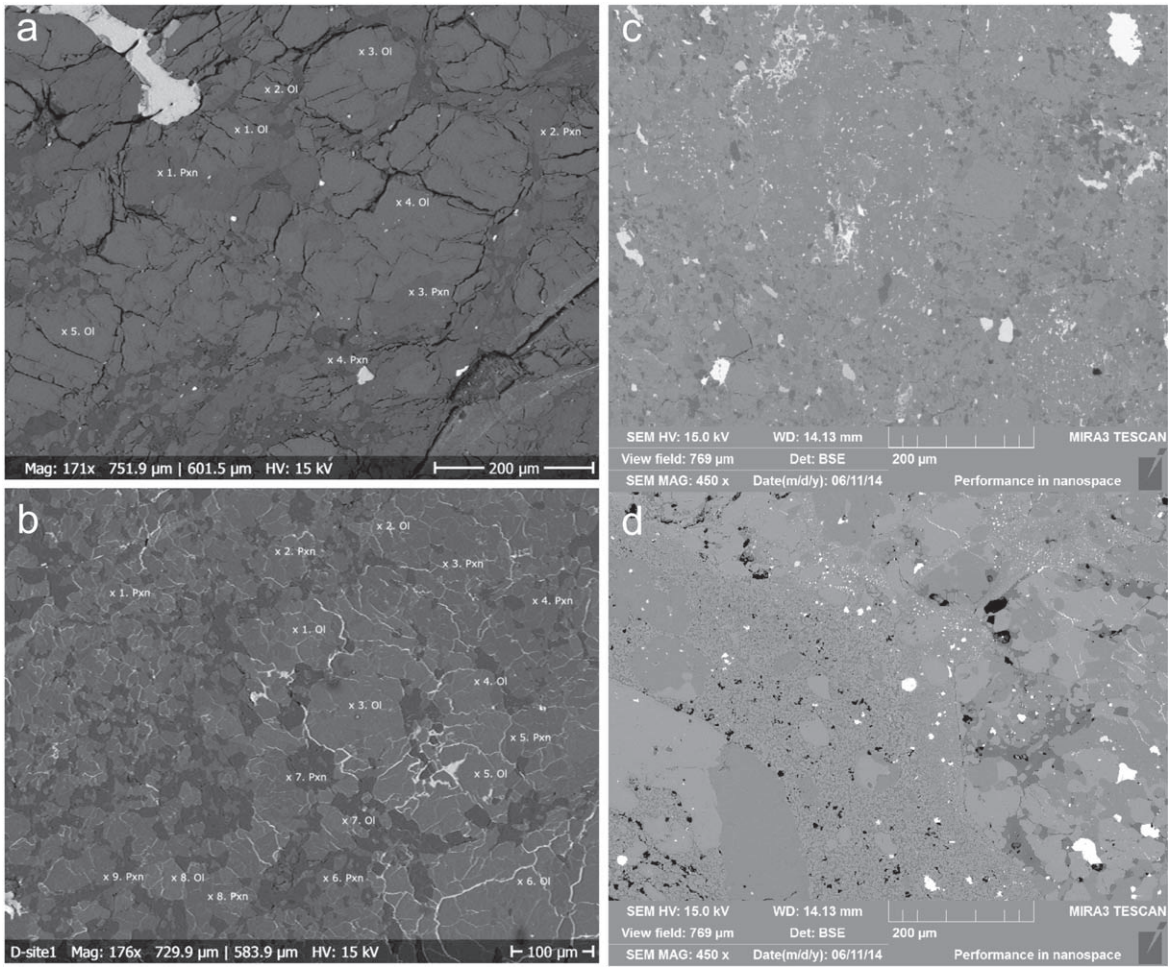

Figure 1. Scanning electron microscope image of the three Chelyabinsk lithologies. (a) Light-colored lithology with mechanically crushed silicate grains, (b) dark-colored lithology with troilite melt-bearing cracks within silicate grains, (c) and (d) impact melt lithology consisting predominantly of whole-rock melt with (c) fine-crushed residual silicate grains and (d) newly crystallized olivine.

a shock level of C-S6-7. X-ray diffraction (XRD) and Raman spectroscopy analyses indicate that the overall mineralogy of the three Chelyabinsk lithologies is similar (Moroz et al. 2014; Reddy et al. 2014; Oshtrakh et al. 2019) with the exception of newly crystallized long prismatic olivine crystals in the IM lithology which are more magnesium rich (Kaeter et al. 2018). For our study, we selected representative powdered samples of all three lithologies from collections at the Ural Federal University, Ekaterinburg, Russia. The scanning electron microscope images in backscattered electrons (SEM-BSE) in Figure 1 were acquired at the Department of Geology and Geography, University of Helsinki, Finland, using a JEOL JXA-8600 Superprobe, and at the Czech Geological Survey using a TESCAN MIRA 3GMU.

2.2. Shock and Space-weathering Simulations

In order to simulate shock effects, we prepared intimate mixtures of fine-grained powdered (grain size 45 μm) mixtures of the Chelyabinsk light-colored lithology with both dark-colored lithology (labeled as SD series; newly prepared; mixing in wt.% steps of 0%, 5%, 10%, 20%, 30%, 40%, 50%, 60%, 70%, 80%, 90%, 95%, and 100% of the dark-colored lithology) and impact melt lithology (IM series; identical to the one used in Reddy et al. (2014) mixing in wt.% steps of 0%, 10%, 20%, 30%, 40%, 50%, 60%, 70%, 80%, 90%, 95%, and 100% of the IM lithology). The light-colored lithology represents the end-member of an unmelted, low-shock material on one side. On the other side, the dark-colored lithology represents a shock-darkened end-member (characterized by the presence of partial troilite melt) of the shock level C-S5-6, and the IM lithology represents a whole-rock melt end-member of the shock level C-S7. Thus, with our areal mixtures, we simulate a progressive increase of shocked and melted materials within ordinary chondrites rather than increases in shock load.

In order to simulate space-weathering, we selected a powdered sample of the light-colored lithology and subjected it to laboratory space-weathering using a two-step thermal treatment method described in detail in Kohout et al. (2014a). The method mimics the optical effects of iron nanoparticles ($npFe^0$) on reflectance spectra of silicate minerals and is based on controlled growth of 5–20 nm-sized $npFe^0$ on the surfaces of powdered silicate mineral grains. Initially, the mineral powders are heated in ambient air to oxidize Fe^{2+} ions on the perimeter of the silicate grains into iron oxide nanoparticles. In the second step, the iron oxide particles are reduced in H_2 atmosphere into $npFe^0$. The temperature of the first heating step is proportional to the $npFe^0$ production yield. Thus, our method simulates a progressive increase of $npFe^0$ amount as a space-weathering product. Temperature steps of 400 °C,

Table 1
Spectral Parameters and PCA Results of the Chelyabinsk Meteorite Series and Three Areas on Asteroid Itokawa

Spectrum	BD1	BD2	BDR	BA1	BA2	BAR	B1C	A	S	PC1	PC2	Class	SWP
SD 0%	0.056	0.023	0.41	0.020	0.010	0.50	0.940	0.25	0.08	−0.5483	0.2599	Q	−0.13
SD 5%	0.047	0.019	0.40	0.017	0.008	0.49	0.940	0.22	0.08	−0.5460	0.2431	Q	−0.12
SD 10%	0.040	0.016	0.40	0.014	0.007	0.48	0.935	0.20	0.08	−0.5455	0.2213	Q	−0.11
SD 20%	0.031	0.012	0.37	0.011	0.005	0.45	0.930	0.18	0.07	−0.5375	0.1783	Q	−0.09
SD 30%	0.025	0.009	0.35	0.009	0.004	0.46	0.925	0.16	0.07	−0.5352	0.1484	Q	−0.08
SD 40%	0.020	0.007	0.36	0.007	0.003	0.46	0.935	0.16	0.06	−0.4978	0.0943	Q	−0.03
SD 50%	0.015	0.006	0.38	0.005	0.002	0.44	0.920	0.13	0.07	−0.5044	0.0780	Q	−0.03
SD 60%	0.013	0.004	0.34	0.005	0.002	0.41	0.935	0.12	0.07	−0.5062	0.0535	Ch/Xn/C/Xk	−0.02
SD 70%	0.009	0.003	0.36	0.003	0.001	0.43	0.955	0.10	0.07	−0.4880	0.0223	Cb	0.00
SD 80%	0.007	0.002	0.35	0.003	0.001	0.46	0.960	0.09	0.08	−0.4638	−0.0054	Cb	0.04
SD 90%	0.005	0.002	0.38	0.002	0.001	0.42	0.985	0.09	0.07	−0.4508	−0.0290	Cb	0.06
SD 95%	0.005	0.002	0.34	0.002	0.001	0.37	0.980	0.08	0.08	−0.4540	−0.0385	Cb	0.06
SD 100%	0.004	0.001	0.38	0.002	0.001	0.48	1.010	0.08	0.07	−0.4373	−0.0541	Cb	0.08
IM 0%	0.054	0.016	0.30	0.021	0.007	0.34	0.945	0.27	0.07	−0.6999	0.2477	Q	−0.27
IM 10%	0.044	0.013	0.29	0.016	0.006	0.34	0.946	0.24	0.08	−0.6739	0.2209	Q	−0.23
IM 20%	0.033	0.009	0.28	0.013	0.004	0.33	0.945	0.21	0.07	−0.6674	0.1891	Q	−0.22
IM 30%	0.028	0.008	0.30	0.010	0.004	0.35	0.948	0.19	0.06	−0.6744	0.1807	Q	−0.22
IM 40%	0.022	0.006	0.27	0.008	0.003	0.32	0.945	0.18	0.06	−0.6432	0.1442	Q	−0.18
IM 50%	0.018	0.005	0.29	0.007	0.003	0.38	0.944	0.15	0.07	−0.6517	0.1403	Q	−0.19
IM 60%	0.013	0.004	0.29	0.005	0.002	0.33	0.945	0.14	0.06	−0.6342	0.1022	Ch/Xn/C/Xk	−0.16
IM 70%	0.011	0.003	0.24	0.005	0.001	0.27	0.949	0.13	0.06	−0.6251	0.0859	Ch/Xn/C/Xk	−0.15
IM 80%	0.008	0.002	0.20	0.003	0.001	0.24	0.949	0.11	0.07	−0.6146	0.0622	Ch/Xn/C/Xk	−0.13
IM 90 %	0.006	0.002	0.28	0.002	0.001	0.29	0.957	0.11	0.06	−0.5774	0.0416	Ch/Xn/C/Xk	−0.09
IM 95%	0.005	0.001	0.23	0.002	0.001	0.26	1.024	0.10	0.07	−0.5637	0.0208	Ch/Xn/C/Xk	−0.07
IM 100%	0.004	0.001	0.34	0.002	0.001	0.35	1.037	0.10	0.08	−0.5738	0.0255	Cb	−0.08
SW 0	0.073	0.030	0.38	0.030	0.014	0.41	0.965	0.25	0.06	−0.7462	0.3798	Q	−0.35
SW 400	0.052	0.025	0.46	0.020	0.011	0.50	0.925	0.18	0.17	−0.4701	0.2329	Q	−0.05
SW 500	0.024	0.014	0.54	0.008	0.006	0.72	0.950	0.12	0.25	−0.2371	0.1310	Sq	0.21
SW 600	0.010	0.006	0.61	0.002	0.002	1.09	0.925	0.07	0.29	−0.1758	0.0225	Sqw	0.30
Itokawa B	0.054	0.010	0.19										
Itokawa HA	0.062	0.012	0.20										
Itokawa MS	0.055	0.011	0.21										

Note. BD1—1 μm band depth; BD2—2 μm band depth; BDR—band depth ratio; BAR—band area ratio; B1C—1 μm band center; A—albedo; S—slope; PC—principal components; SWP—space-weathering parameter; SD—shock-darkening mixture series, the value indicates the amount of SD material; IM—impact-melting mixture series, the value indicates the amount of IM material; SW—space-weathering mixture series, the value in brackets indicates thermal treatment temperature; Itokawa B—boulder-rich area; Itokawa HA—high-albedo area; Itokawa MS—Muses Sea.

500 °C, and 600 °C were selected to form (together with fresh pristine material) a simulated space-weathering series (labeled SW series).

The complete list of samples used in this study is presented in Table 1.

2.3. Reflectance Spectrum Measurements

The reflectance spectral measurement of the SD and SW series samples was carried out over the range of 400–2500 nm using an OL-750 automated spectroradiometric measurement system by Gooch & Housego located at the Department of Physics, University of Helsinki. The OL-750 instrument is equipped with a polytetrafluoroethylene (PTFE) integrating sphere with a specular reflection trap and measures hemispherical reflectance. The spectra were measured relative to a PTFE standard. The spectral resolution of the instrument varies between 5 and 10 nm.

The spectral measurement of the IM series is identical to those presented previously in Reddy et al. (2014) and was carried out over an identical wavelength range using an Analytical Spectral Devices FieldSpec Pro HR spectrometer at the Centre for Terrestrial and Planetary Exploration (C-TAPE), University of Winnipeg. The FieldSpec Pro measures a bidirectional reflectance with a viewing geometry of incidence angle $i = 30°$ and emergence angle $e = 0°$. The spectra were measured relative to an NIST-traceable LabSphere Spectralon standard. A total of 500 spectra of the sample, target, and dark current were acquired to improve signal to noise. The spectra were corrected for minor irregularities in Spectralon's absolute reflectance beyond ~2000 nm, as well as occasional small reflectance offsets at 1000 and 1830 nm, where detector changeovers occur. The spectral resolution of the instrument varies between 2 and 7 nm, and data are internally processed by the spectrometer to output data at 1 nm intervals.

In both instruments, the illumination was provided using a collimated tungsten lamp. The SD series was measured using both devices, and the reflectance values from both instruments were found to be in agreement within 10% and thus comparable. The relative error in reflectance values (determined through repeated measurements) presented in Figure 2 is

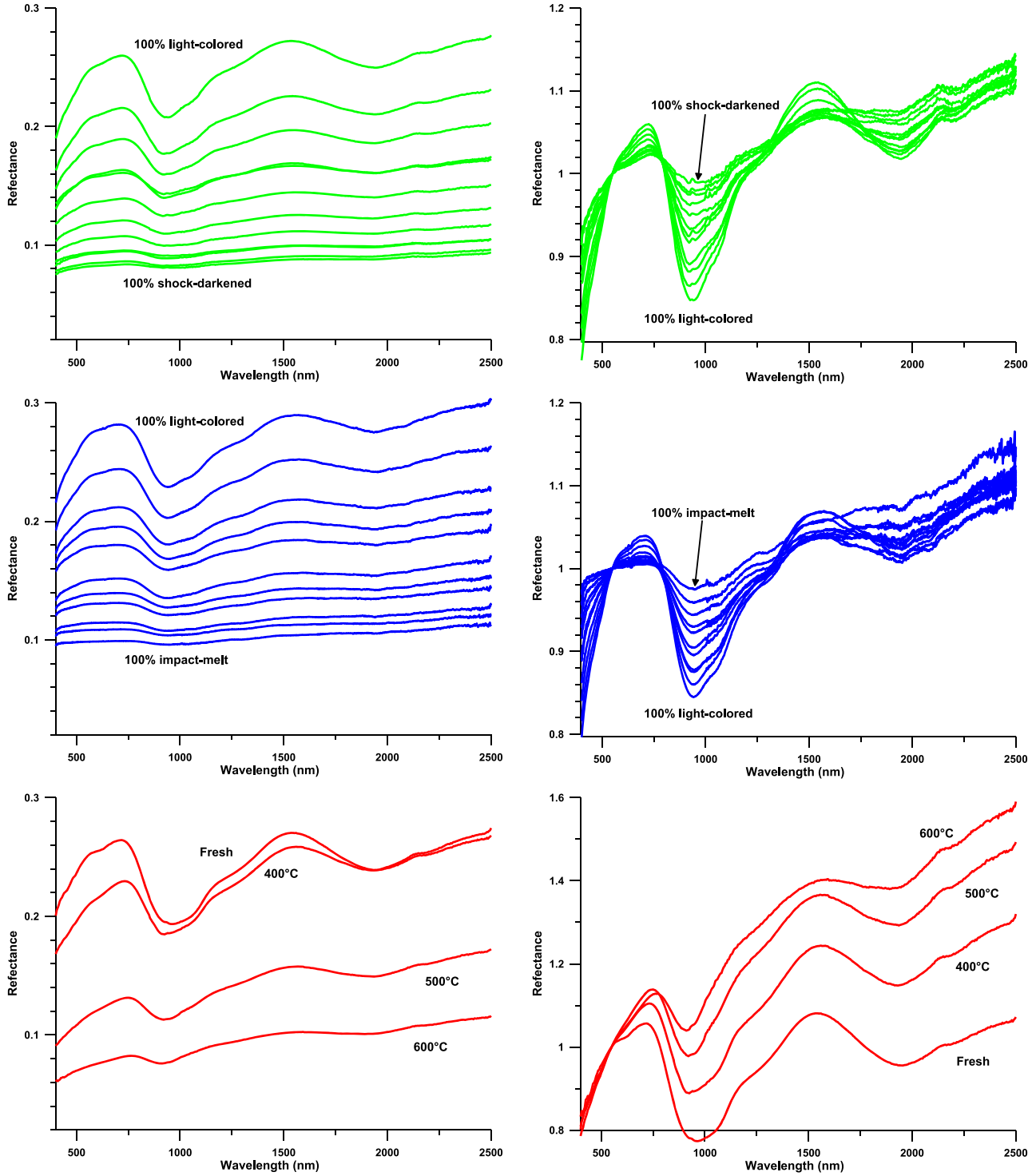

Figure 2. Raw (left) and normalized (right) spectra of the SD (top), IM (middle), and SW (bottom) series.

~3%. The absolute error of the values in Figures 3–9 is approximately the same as the data point symbol size. The maximum expected error in wavelength position is approximately twice the measurement step and is ~14 nm in the case of FieldSpec Pro HR and ~20 nm in the case of OL-750.

2.4. Spectral Processing and Classification

Both meteorite and asteroid spectra were processed in the following steps. In order to determine the band depth and band area at 1 and 2 μm, a linear continuum was fitted over the bands as a linear line connecting the local maxima at each shoulder of the band depth. For the 2 μm band, we used the reflectance value at 2.48 μm as a right shoulder. Subsequently, the band depth was determined as a reflectance difference between the continuum and the band center. The band center was determined simply as the wavelength position of the local minimum of the continuum-removed spectral curve. The band area was similarly determined as the area outlined by the

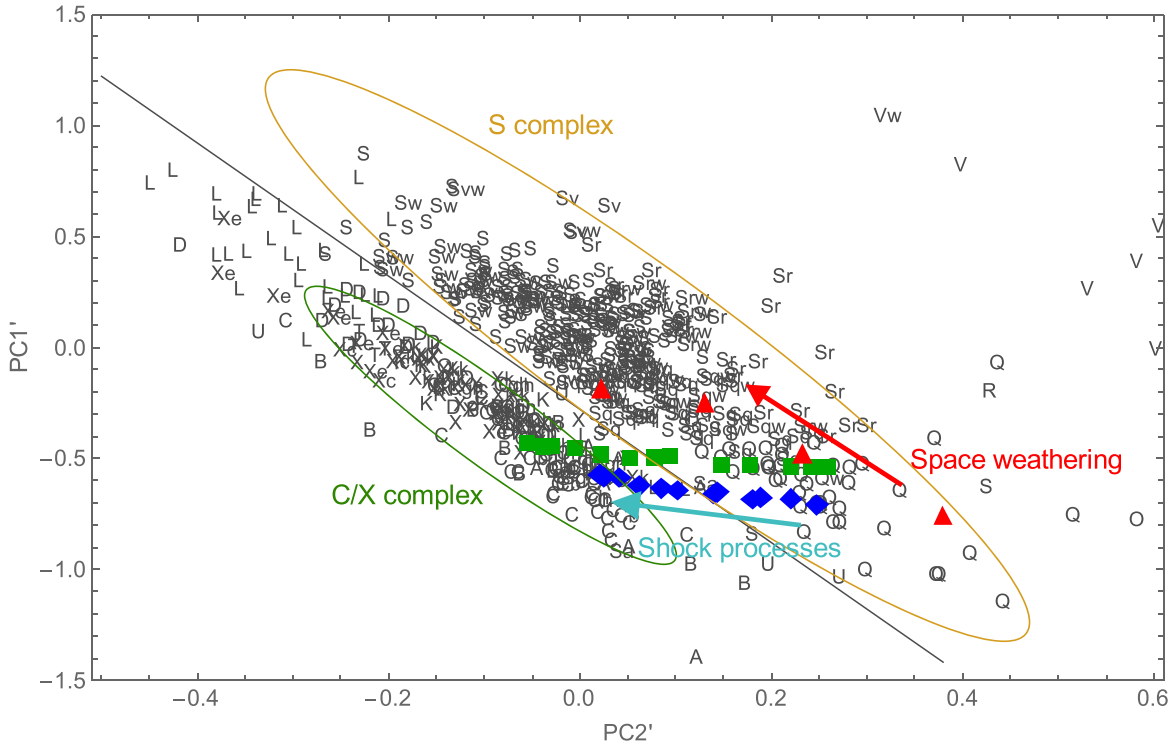

Figure 3. Shock (SD series—green squares, and IM series—blue diamonds) and space-weathering (SW series—red triangles) trends as seen in the principal component analysis (PCA) space. The figure background is modified from Binzel et al. (2019). The letters indicate the asteroids and their taxonomies from the DeMeo et al. (2009) main-belt asteroid data and the MITHNEOS near-Earth asteroid data from Binzel et al. (2019). S-complex and C/X-complex clouds are outlined for clarity.

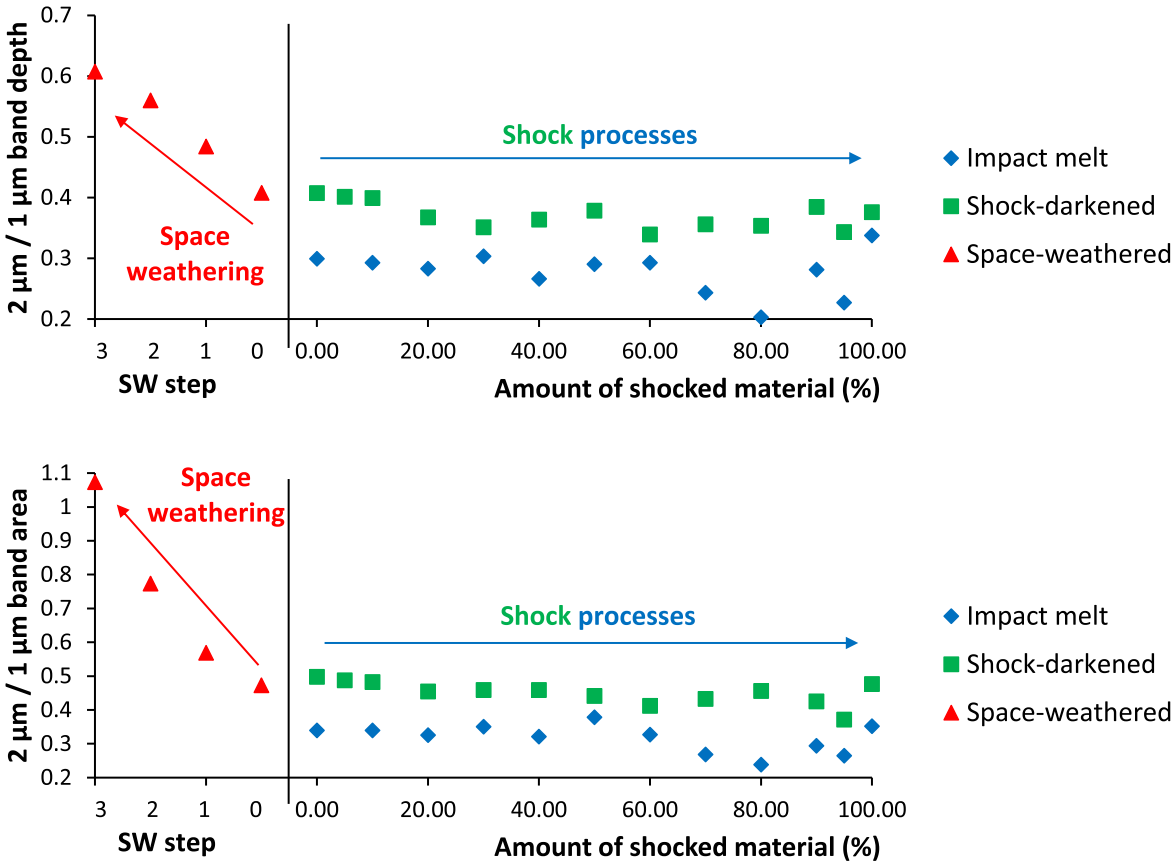

Figure 4. BDR—the ratio of the 2 μm to 1 μm band depths (top) and BAR—the ratio of the 2 μm to 1 μm band areas (bottom) as a function of the abundance of shock-darkened or impact-melted material, or intensity of laboratory-produced space-weathering.

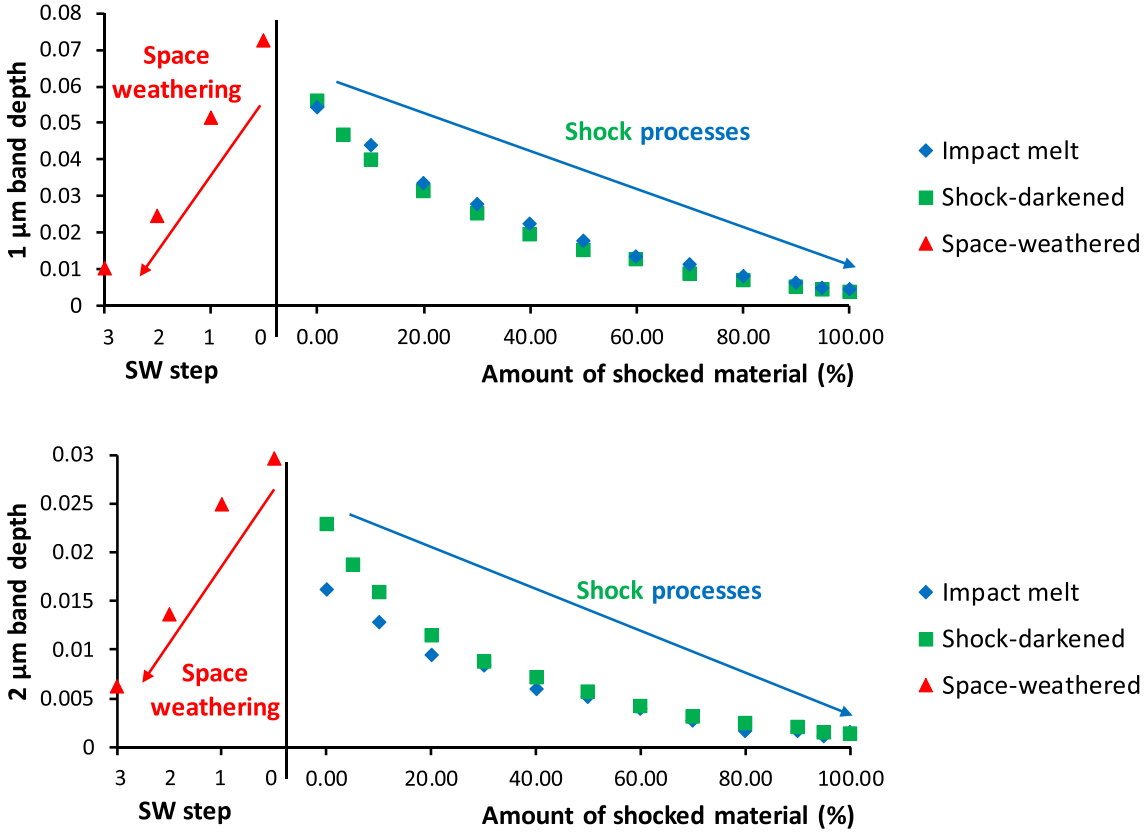

Figure 5. The 1 μm (top) and 2 μm (bottom) band depths as a function of the amount of shock-darkened or impact-melted material, or intensity of laboratory-produced space-weathering.

absorption band as the lower boundary and the continuum as the upper boundary. The albedo was determined as the reflectance at 550 nm. We note that the band amplitude in highly shocked samples approaches noise levels, and the absorption bands become poorly constrained. This is reached for the weaker 2 μm band in the SD series at 70% shock-darkened material amount and in the IM series at 60% impact-melted material amount. The 2 μm band in the SW series, as well as the 1 μm band in all samples, is always above the noise level. The noise level was estimated as 3% of the relative reflectance measurement error of the albedo value. To calculate normalized spectra, reflectance normalization to unity was done at 550 nm. Additionally, all presented spectra were classified using the online Bus–DeMeo PCA (principal component analysis) taxonomy calculator (http://smass.mit.edu/busdemeoclass.html). The automated procedure smooths the uploaded spectrum using a cubic spline, normalizes it to unity at 0.55 μm, determines and subtracts the overall slope, calculates PCA components, and then assigns a Bus–DeMeo classification (DeMeo et al. 2009; Binzel et al. 2019) using the PC values and predetermined spectral slope.

2.5. Itokawa Asteroid Spectra

In order to compare our meteorite-based results to asteroid material, representative spectra of three typical areas on asteroid 25143 Itokawa—a boulder-rich area, a high-albedo area, and the Muses Sea area—were obtained in the range of 0.75–2.1 μm from Figure 7 in Abe et al. (2006). The 1 μm and 2 μm band depths were calculated as a difference between local band minima and local maximum at 1.7 μm because of the limited spectral range of the Hayabusa data (i.e., incomplete coverage of the absorption bands). Due to this reason, it was not possible to calculate the band areas as the bands are not fully covered within the published spectral data.

3. Results

The measured spectra of all three Chelyabinsk meteorite series are shown in Figure 2. A gradual attenuation of both 1 μm and 2 μm silicate absorption bands can be observed with increasing amounts of shock-darkening or impact-melting (SD and IM series), as well as with simulated space-weathering (SW series). The SD and IM series do not show any significant slope change nor systematic trend in the 1 μm band minima position (Table 1) as a function of shocked or melted material abundances up to amounts of 80 wt.%. At high shocked material abundances, the absorption bands became poorly constrained due to their amplitude being at the noise level as outlined in Section 2.4. Thus, the spectral parameters in Table 1 for highly shocked samples should be considered with caution.

The calculated spectral parameters together with the PCA results are listed in Table 1. The results of the PCA analysis are presented in Figure 3. As can be seen from Figure 3 and Table 1, the spectrum of the light-colored Chelyabinsk lithology with low amounts of shocked or melted (SD and IM) materials is characterized as a Q type within the S complex, consistent with its fresh ordinary chondrite composition. At shocked or melted material amounts over 60%, the spectrum classification changes to the C/X complex. The classification results of the shock-darkened-rich and impact-melt-rich materials indicate transition from Q type through Ch/Xn/C/Xk (ordered by the Bus–DeMeo PCA taxonomy

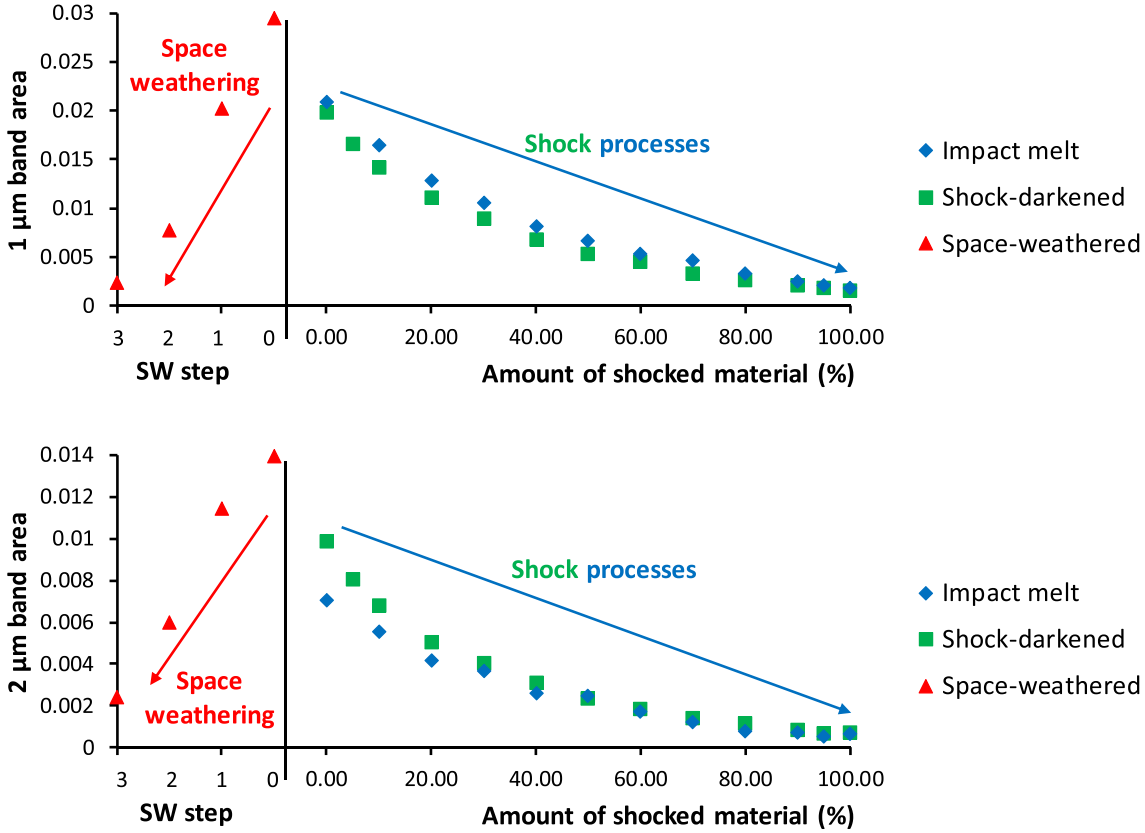

Figure 6. The 1 μm (top) and 2 μm (bottom) band areas as a function of the amount of shock-darkened or impact-melted material or intensity of laboratory-produced space-weathering.

calculator fit confidence) toward Cb-like reflectance spectra. In contrast, the SW series takes a different path, and the spectra of the individual members stay within the S complex, forming a Q/Sq/Sqw track.

To further study the effect of shock, melt, or space-weathering on individual silicate absorption bands, we calculated and plotted the ratio of the 2 μm to 1 μm band depths (BDR) and band areas (BAR) against the amount of shocked, melted, or space-weathered material (Figure 4) together with the behavior of individual band depths and band areas (Figures 5 and 6). The results indicate (1) a progressive decrease of both individual band depths and band areas in all three SD, IM, and SW series, (2) little variation in the BDR and BAR of both SD and IM series as a function of the increasing proportion of shocked or melted material, and (3) a progressive increase in the BDR and BAR with simulated space-weathering in the SW series. The observed trends in the BDRs are identical to those in BARs in all three series. In Figure 7, the BDR, BAR, and space-weathering parameter (SWP) are plotted also against the slope. SWP is described in Binzel et al. (2019) and quantifies how far a given S-complex spectrum is from the Q/S boundary in the PC1′–PC2′ space. Positive values indicate S-type spectra while negative values indicate Q-type spectra.

Figure 8 outlines the individual 1 μm and 2 μm band depths and slope behavior of our samples as a function of albedo, similar to the graphs in Gaffey (2010) for the Moon, asteroid 243 Ida, and asteroid 433 Eros. One can observe that all three materials behave similarly in the band depths versus albedo plots, but the SW series is distinct in the slope versus albedo plot from the SD and IM series.

Results from the three typical areas on asteroid 25143 Itokawa—a boulder-rich area, a high-albedo area, and the Muses Sea areas presented in Abe et al. (2006)—indicate almost no variation in the BDR (Table 1).

4. Discussion

The three experimentally prepared material series from the Chelyabinsk meteorites allow us to quantitatively compare the effect of increasing proportion of shock-darkened material (SD series) and impact-melted material (IM series) to the increasing level of space-weathering (SW series) on ordinary chondrite reflectance spectra. Several trends can be observed. The general behavior of both albedo and absorption band depths (reduction with increasing amounts of shocked or melted materials and space-weathering) is consistent with previous studies (e.g., Britt & Pieters 1994; Keil et al. 1992, and Reddy et al. 2014 for shock; or Brunetto et al. 2006; Marchi et al. 2005, and Sasaki et al. 2001, 2003 for space-weathering) and our expectations as outlined in the Introduction. However, SW also shows an increase in spectral slope, unlike the trend in the SD and IM series. Furthermore, as seen from Figure 2, we can conclude that the spectral changes related to the shock-darkened material (SD, partial melting of troilite and metal) and to the impact-melted material (IM, whole-rock melting and metal/troilite redistribution) are similar. From Table 1 it is apparent that at 60% admixture of shocked material, the reflectance spectra transitions from the S complex into the C/X complex across the boundary alpha line defined in DeMeo et al. (2009). The highly shocked or melted end-members are classified as Cb (with typical neutral or negative spectral slope), revealing a

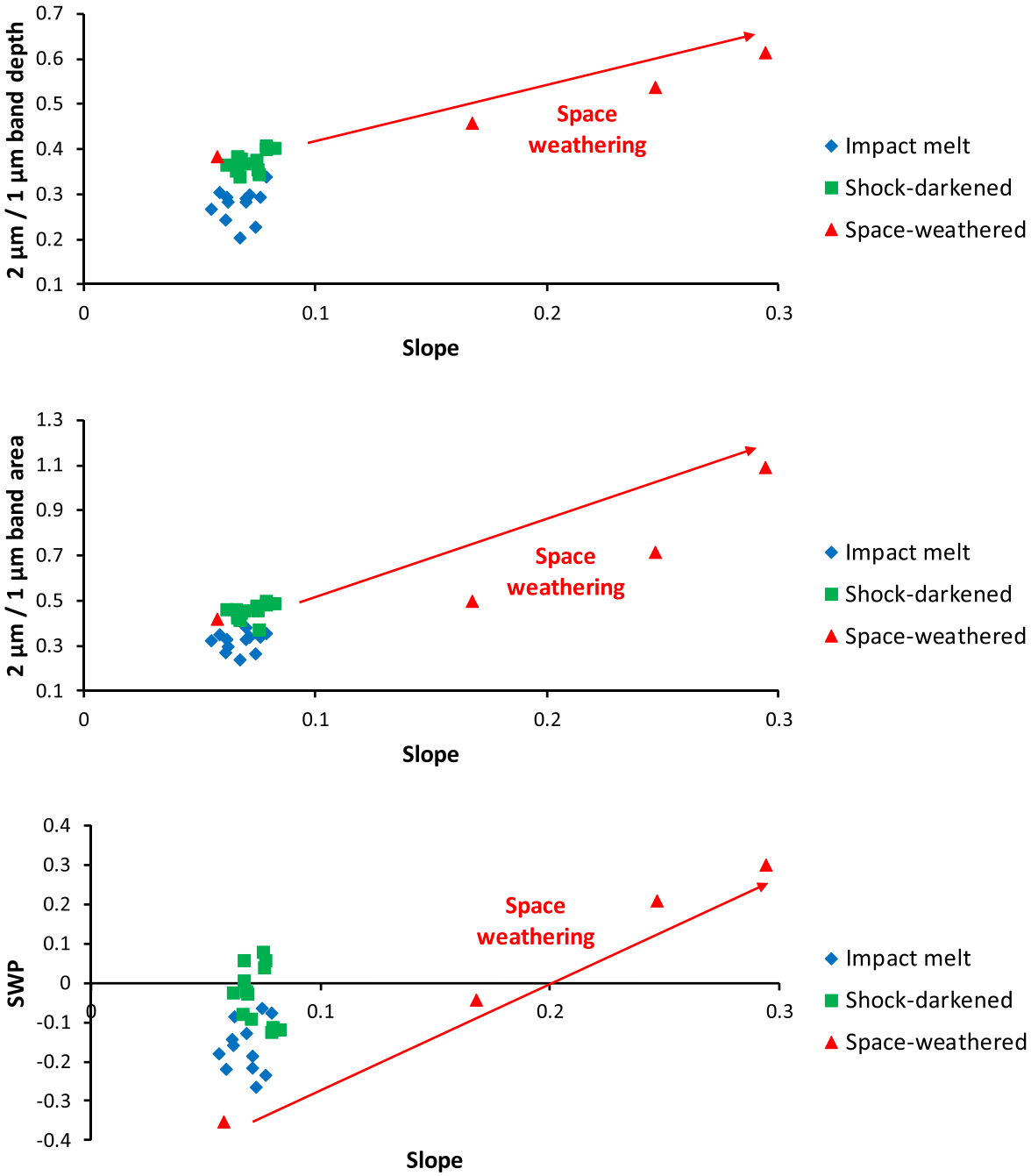

Figure 7. BDR—the ratio of the 2 μm to 1 μm band depths (top), BAR—the ratio of the 2 μm to 1 μm band areas (middle), and space-weathering parameter SWP (bottom) as a function of spectral slope—see text for the definition of spectral slope and SWP.

lack of reddening typical for space-weathering. In contrast, the increase in space-weathering results in significant slope change (Figure 2) and reflectance spectra transition from Q toward Sq/Sqw. The combined graphical representation of the SD, IM, and SW trends in PCA space is depicted in Figure 3 (modified from Binzel et al. (2019). From this figure, we can further conclude that our SW series is consistent with the space-weathering vector, while the SD and IM series are consistent with the shock vector presented in (Binzel et al. 2019).

The slope behavior or the different paths taken by the different meteorite mixture series spectra in the PCA classification are not the only observed difference between the space-weathering and shock-associated spectral effects. The ratios of the 2 μm to 1 μm band depths (BDR) and of the 2 μm to 1 μm band areas (BAR) are both almost constant in the SD and IM series (Figure 4) but show significant increases with the amount of space-weathering in the SW series. The constant BDR and BAR are explained by an equivalent relative attenuation of both bands with an increase of the shock-darkened and impact-melted material proportions in the SD and IM series. In contrast, the increase of the same BDR and BAR parameters in the SW series is a consequence of relatively more progressive attenuation of the 1 μm band with increasing simulated space-weathering compared to the 2 μm band. We interpret this behavior as a direct consequence of the faster response of olivine to space-weathering compared to orthopyroxene as suggested earlier by Sasaki et al. (2002), Quadery et al. (2015), and Marchi et al. (2005). The 2 μm band is

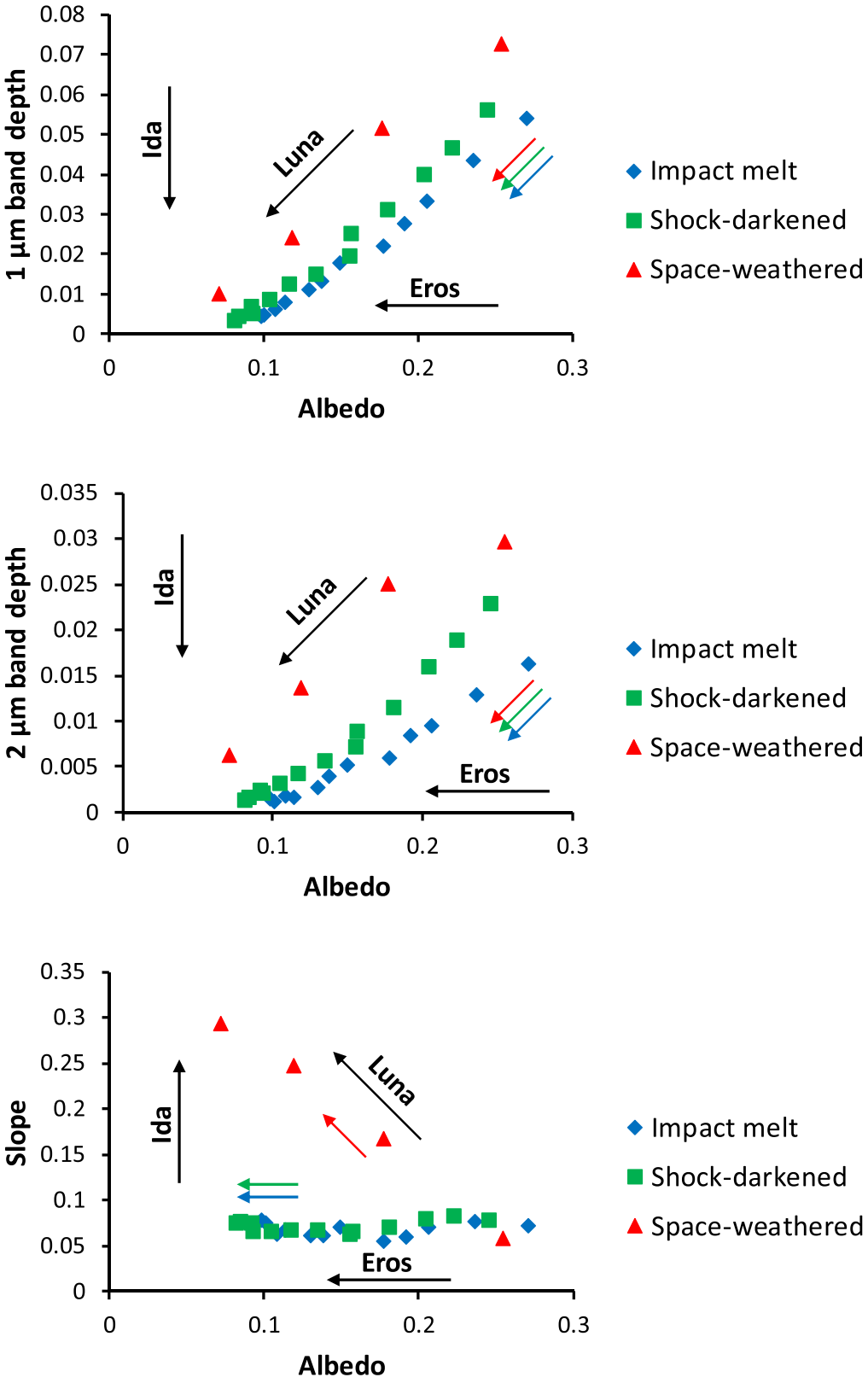

Figure 8. The 1 μm (top) and 2 μm (middle) band depths and slope (bottom) as a function of albedo. The asteroidal and lunar trends are after Gaffey (2010).

dominated by more resistant orthopyroxene while the 1 μm band is also contributed to by less resistant olivine, which shows a faster response to space-weathering. This is further supported by a strong linear correlation between the 2 μm to 1 μm BDR or BAR and the slope in the SW series (Figure 7), further strengthening the link between the BDR or BAR and space-weathering. The "non-weathered" SD and IM series data points group more tightly in the BDR or BAR versus slope plot than in the similar SWP versus slope plot. This means that the 2 μm to 1 μm BDR and BAR are more sensitive to distinguish

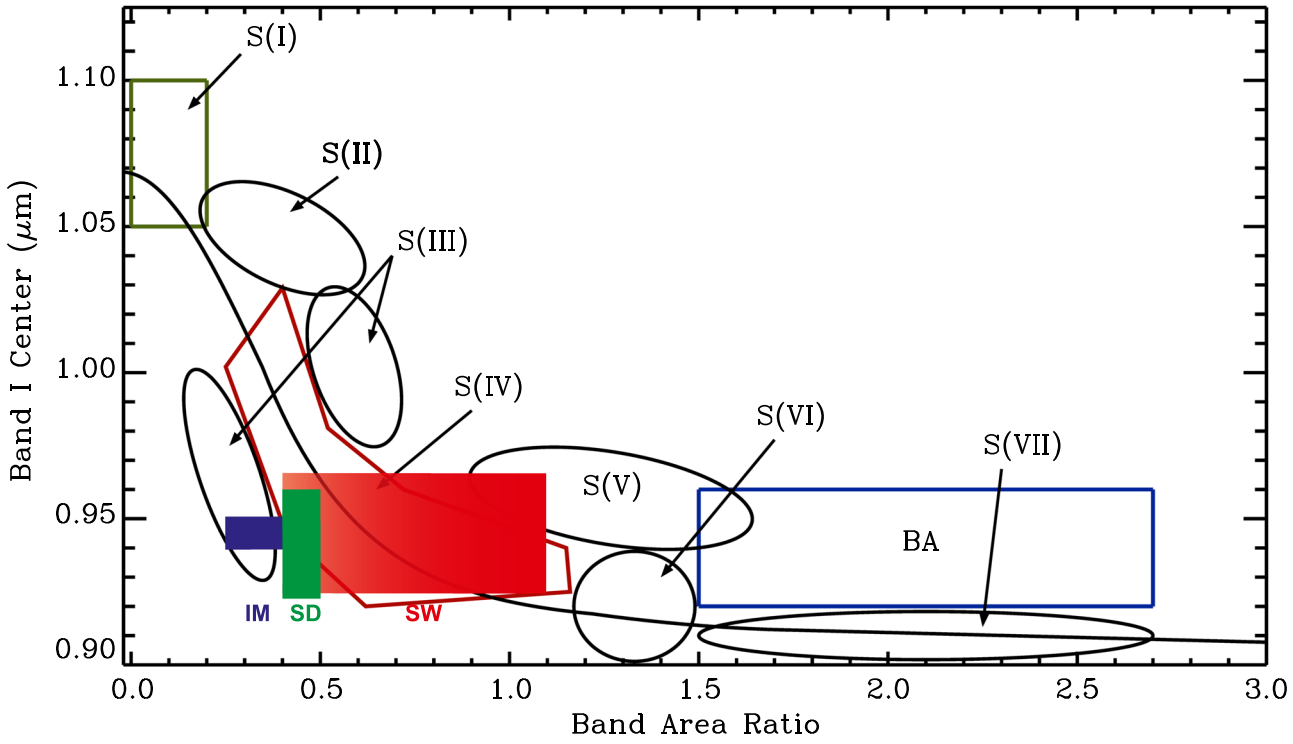

Figure 9. Band I center vs. BAR plot from Gaffey et al. (1993) with areas of S asteroid subtypes S(I)–S(VII), pyroxene-rich basaltic asteroids (BA), and our IM, SD, and SW data clouds. The space-weathering progression along the BAR axis and the olivine–orthopyroxene mixing line (black curve) is indicated by the SW rectangle red color gradient.

space-weathering trends from shock processes in reflectance spectra than the SWP.

Another consequence of this study is that shock processes are more efficient in "erasing" the orthopyroxene signature manifested by the 2 μm absorption than space-weathering. As the 2 μm absorption is strongly correlated to PC2′ (principal component 2) and the diagnostic of the S complex in the PCA taxonomy, shock processes obstructing this feature are more likely to be able to mask the silicate asteroid compositions, rendering them as the C/X-complex spectra.

The band area calculation is often used to determine asteroid composition in the Band I center versus BAR plots (Cloutis et al. 1986; Gaffey et al. 1993). In Figure 9 we plot our data on the figure from Gaffey et al. (1993). We are aware of the relatively larger scatter of the SD and SW series Band I center values compared to those of the IM series. We attribute this to the lower spectral resolution of the OL-750 instrument used to measure the SD and SW samples and related noise in the data being responsible for larger (~20 nm) uncertainties in the local minima position. Based on Figure 9 and Table 1, we can state that shock processes (IM and SD series) do not produce any systematic trends in the Band I center versus BAR plot and thus, do not significantly distort the asteroid composition derived from this figure. In the case of the space-weathering (SW series), a notable trend is observed along the BAR axis and the olivine–orthopyroxene mixing line mainly due to a systematic shift in the BAR values. The shift can distort the spectrally derived apparent material composition contrary to previous assumptions (e.g., Gaffey 2010). Despite this, the SW series spectra still stay within the S(IV)-type area, being similar to ordinary chondrites. This effect has to be taken into account in asteroid spectral analysis. The S-type asteroids are possibly more sensitive to the shift in the Gaffey plot as they contain both olivine and orthopyroxene in significant proportions and thus, are sensitive to the different weathering rates of these minerals compared to the V-types which are spectrally dominated by a single mineral—orthopyroxene.

From Figure 8, which is based on plots by Gaffey (2010), it can be seen that both shock (SD and IM) and space-weathering (SW) trends follow lunar-type space-weathering in the behavior of the 1 μm and 2 μm band depths with albedo. The space-weathering is also consistent with the lunar trend in the slope versus albedo plot. The shocked and melted materials, however, do not show any pronounced slope changes and are like trends observed on the asteroid Eros in the slope versus albedo plot (Gaffey 2010). Thus, shock effects can partly explain the deviation of observed spectral trends on Eros from those on the Moon. We cannot, however, rule out other reasons for the Eros spectral variations such as, for example, surface roughness effects.

Finally, we analyzed three representative spectra of various areas on the asteroid Itokawa to search for variation attributable to space-weathering. We did not find significant variation in the BDR. The boulder-rich area, high-albedo area, as well as the fine-grained and similarly bright Muses sea area have consistent BDRs—in the range of 1.9–2.1. This suggests that Itokawa is rather uniformly space-weathered, and surface roughness, grain size variations, or relative albedo variations do not influence the BDR.

5. Conclusions

As demonstrated for the Chelyabinsk meteorite, the 2 μm to 1 μm band depth ratio (BDR) as well as the 2 μm to 1 μm band

area ratio (BAR) are not appreciably affected by shock-darkening or shock melting. Space-weathering, however, causes significant shifts in both BDR and BAR toward higher values. BDR and BAR calculation is not based on spectral slope, and the resulting values are independent of spectral normalization. The BDR and BAR shift during space-weathering is explained due to the relatively more progressive attenuation of 1 μm absorption contributed by olivine relative to the 2 μm of orthopyroxene. The shock processes do not cause significant spectral slope changes and are more efficient in attenuating the orthopyroxene 2 μm absorption band, resulting in distinct shock-darkening and impact-melting vectors in the reflectance spectra PCA space compared to the space-weathering vector. More specifically, the disappearance of the 2 μm absorption band moves the shocked silicate-rich Chelyabinsk spectra from the S-complex space into the C/X complex, while space-weathered material stays within the S complex, moving from Q type to S type. Application of the BDR method to the three distinct areas on the asteroid Itokawa reveals that Itokawa is rather uniformly space-weathered.

Thus, BDR and BAR can be used as reliable indicators to distinguish relative spectral changes caused by the shock due to space-weathering within materials of the same overall composition. Space-weathering produces a significant shift along the BAR axis and the olivine–orthopyroxene mixing line in the Band 1 center versus BAR plot for S-complex asteroids. This effect has to be considered when deriving asteroid compositions from these plots.

6. Supplementary Data File

Raw spectra of the Chelyabinsk IM, SD, and SW series can be found at [doi:10.5281/zenodo.3954347].

We would like to thank Juan Sanchez for his help with PCA classification, Radoslaw Michallik for his help with the SEM images, and Eric MacLennan for his help with digitizing Figure 9. This research is supported by the Academy of Finland project No. 293975 and the Ministry of Education, Youth and Sports of the Czech Republic grant No. LH12079, NASA SSERVI Center for Asteroid and Lunar Surface Science (CLASS), MINOBRNAUKI project 5.3451.2017/4.6, Minobrnauki project FEUZ-2020-0059, and Act 211 of the Government of the Russian Federation, agreement No. 02. A03.21.0006, and with institutional support RVO 67985831 of the Institute of Geology of the Czech Academy of Sciences. The University of Winnipeg's C-TAPE was established with funding from the Canada Foundation for Innovation, the Manitoba Research Innovation Fund, the Natural Sciences and Engineering Research Council of Canada (NSERC), the Canadian Space Agency, and the University of Winnipeg. This study was supported with funding from NSERC.

ORCID iDs

Tomas Kohout https://orcid.org/0000-0003-4458-3650
Ed Cloutis https://orcid.org/0000-0001-7301-0929
Vishnu Reddy https://orcid.org/0000-0002-7743-3491

References

Abe, M., Takagi, Y., Kitazato, K., et al. 2006, Sci, 312, 1334
Adams, J. B., & Jones, R. L. 1970, Sci, 167, 737
Andronikov, A. V., Andronikova, I. E., & Hill, D. H. 2015, P&SS, 118, 54
Bennett, C. J., Pirim, C., & Orlando, T. M. 2013, ChRv, 113, 9086
Binzel, R. P., DeMeo, F. E., Turtelboom, E. V., et al. 2019, Icar, 324, 41
Britt, D. T., & Pieters, C. M. 1994, GeCoA, 58, 3905
Britt, D. T., Pieters, C. M., Webb, R. S., & Pratt, S. F. 1989, LPI, 20, 111
Britt, D. T., Tholen, D. J., Bell, J. F., & Pieters, C. M. 1992, Icar, 99, 153
Brunetto, R., Romano, F., Blanco, A., et al. 2006, Icar, 180, 546
Burns, R. 1993, Mineralogical Applications of Crystal Field Theory (Cambridge: Cambridge Univ. Press)
Burns, R. G. 1970, AmMin, 55, 1608
Chapman, C. R. 2004, AREPS, 32, 539
Cloutis, E. A., Gaffey, M. J., Jackowski, T. L., & Reed, K. L. 1986, JGRB, 91, 1641
DeMeo, F. E., Binzel, R. P., Slivan, S. M., & Bus, S. J. 2009, Icar, 202, 160
Domingue, D. L., Chapman, C. R., Killen, R. M., et al. 2014, SSRv, 181, 121
Gaffey, M. J. 2010, Icar, 209, 564
Gaffey, M. J., Bell, J. F., Brown, R. H., et al. 1993, Icar, 106, 573
Galimov, E. M., Kolotov, V. P., Nazarou, M. A., et al. 2013, GeocI, 51, 522
Grokhovsky, V. I., Muftakhetdinova, R. F., Yakovlev, G. A., et al. 2020, P&SS, in press
Hapke, B. 2001, JGRE, 106, 10039
Hapke, B., Cassidy, W., & Wells, E. 1975, Moon, 13, 339
Hapke, B. W., Cohen, A. J., Cassidy, W. A., & Wells, E. N. 1970, Sci, 167, 745
Heymann, D. 1967, Icar, 6, 189
Hiroi, T., Abe, M., Kitazato, K., et al. 2006, Natur, 443, 56
Kaeter, D., Ziemann, M. A., Böttger, U., et al. 2018, M&PS, 53, 416
Keil, K., Bell, J. F., & Britt, D. T. 1992, Icar, 98, 43
Kohout, T., Čuda, J., Filip, J., et al. 2014a, Icar, 237, 75
Kohout, T., Gritsevich, M., Grokhovsky, V. I., et al. 2014b, Icar, 228, 78
Kohout, T., Petrova, E. V., Yakovlev, G. A., et al. 2020, A&A, 639, 146
Lazzarin, M., Marchi, S., Moroz, L. V., et al. 2006, ApJL, 647, L179
Marchi, S., Brunetto, R., Magrin, S., Lazzarin, M., & Gandolfi, D. 2005, A&A, 443, 769
Moreau, J., Kohout, T., & Wunnemann, K. 2017, M&PS, 52, 2375
Moreau, J. G., Kohout, T., Wuennemann, K., Halodova, P., & Haloda, J. 2019, Icar, 332, 50
Morlok, A., Bischoff, A., Patzek, M., Sohn, M., & Hiesinger, H. 2017, Icar, 284, 431
Moroz, T. N., Goryainov, S. V., Pokhilenko, N. P., & Podgornykh, N. M. 2014, DokES, 457, 831
Noble, S. K., Keller, L. P., & Pieters, C. M. 2010, M&PS, 45, 2007
Noguchi, T., Nakamura, T., Kimura, M., et al. 2011, Sci, 333, 1121
Oshtrakh, M. I., Maksimova, A. A., Chukin, A. V., et al. 2019, AcSpA, 219, 206
Pieters, C. M., & Noble, S. K. 2016, JGRE, 121, 1865
Popova, O. P., Jenniskens, P., Emel'yanenko, V., et al. 2013, Sci, 342, 1069
Quadery, A. H., Pacheco, S., Au, A., et al. 2015, JGRE, 120, 643
Reddy, V., Sanchez, J. A., Bottke, W. F., et al. 2014, Icar, 237, 116
Righter, K., Abell, P., Agresti, D., et al. 2015, M&PS, 50, 1790
Rubin, A. E. 1985, RvGeo, 23, 277
Rubin, A. E. 1992, GeCoA, 56, 1705
Sasaki, S., Hiroi, I., Nakamura, K., et al. 2002, AdSpR, 29, 783
Sasaki, S., Kurahashi, E., Yamanaka, C., & Nakamura, K. 2003, AdSpR, 31, 2537
Sasaki, S., Nakamura, K., Hamabe, Y., Kurahashi, E., & Hiroi, T. 2001, Natur, 410, 555
Scott, E. R. D. 1982, GeCoA, 46, 813
Smith, B. A., & Goldstein, J. I. 1977, GeCoA, 41, 1061
Stoffler, D., Hamann, C., & Metzler, K. 2018, M&PS, 53, 5
Stoffler, D., Hamann, C., & Metzler, K. 2019, M&PS, 54, 946
Trieloff, M., Korochantseva, E. V., Buikin, A. I., et al. 2018, M&PS, 53, 343